

NIR filter transformations across the HR diagram: JWST, Roman, and Euclid

M. J. DURBIN,¹ R. L. BEATON,^{2,3} A. J. MONSON,⁴ AND B. SWIDLER⁵

¹Department of Astronomy, University of California, Berkeley, Berkeley, CA, 94720, USA

²Space Telescope Science Institute, Baltimore, MD, 21218, USA

³Department of Physics and Astronomy, Johns Hopkins University, Baltimore, MD 21218, USA

⁴Department of Astronomy/Steward Observatory, University of Arizona, 933 North Cherry Avenue, Tucson, AZ 85721, USA

⁵AFWERX, Air Force Research Laboratory, Wright-Patterson AFB, Dayton, Ohio, USA

ABSTRACT

We present new color transformations between select near-infrared filters on *JWST*/NIRCam, *Euclid*/NISP, *Roman*/WFI, *HST*, and ground-based *izY+IJKS*, for a total of 105 unique filter combinations. Additionally, we apply these transformations to predict the color-magnitude relation of the tip of the red giant branch as seen with *JWST*, *Euclid*, and *Roman* based on theoretical results for *HST* and 2MASS filters; for *JWST* we find good agreement with empirical results in the literature. We also find typical residual dispersion around these transformations of 0.01 mag for Cepheid and RR Lyrae variables and RGB stars, but up to 0.1 mag for O- and C-rich TP-AGB stars.

Keywords: Calibration (2179), infrared astronomy (786), photometric systems (1233), stellar colors (1590), stellar populations (1622)

1. INTRODUCTION

Near-infrared (NIR) spectrophotometry of stars is becoming increasingly crucial for a variety of astrophysical studies. Recent and upcoming missions that operate predominantly in the NIR, such as *JWST* (J. Rigby & et al. 2023), *Euclid* (Euclid Collaboration et al. 2024), and *Roman* (R. Akeson et al. 2019), are expected to observe many more stars with greater accuracy and at farther distances than any previous missions by the end of their lifetimes. *Euclid* and *Roman* in particular are survey telescopes covering large areas of the sky, and as such are designed to accommodate a wide range of scientific use cases in addition to their key projects.

Unlike their ground-based counterparts, spaceborne observatories are not constrained by atmospheric transmission windows, and may access the full range of NIR wavelengths. This can result in substantially greater variations than expected between bandpasses that nominally correspond to the same ground-based filter. *Euclid* and *Roman* specifically are optimized for continuous wavelength coverage, in part for SED reconstruction and photometric redshift measurement. This is illustrated in

Figure 1, which compares throughput curves for all the facilities we consider in this paper.

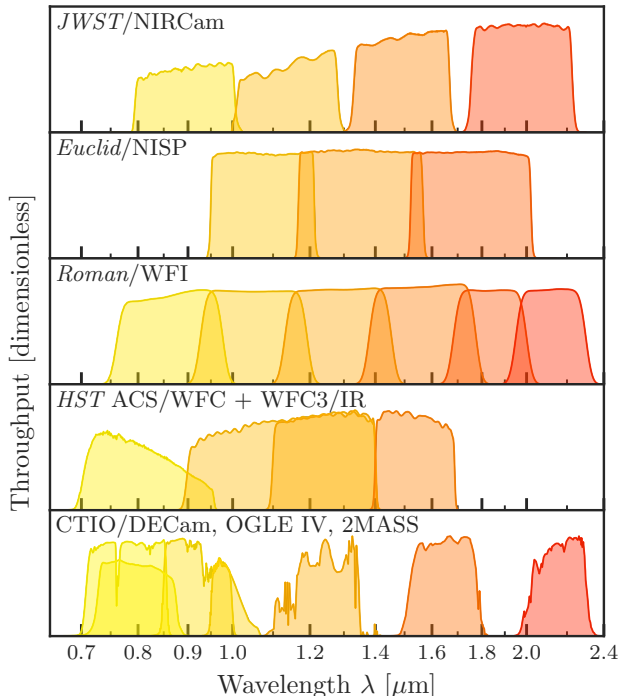


Figure 1. Throughput curves for all filters considered in this work.

Corresponding author: Meredith Durbin
meredith.durbin@berkeley.edu

This paper is a companion to M. J. Durbin et al. (2023), which focused on transformations between WFC3/IR and 2MASS. Here we extend the methods and data presented there to newer and upcoming missions, for which interest in joint calibration is high (e.g. R. Chary et al. 2020; B. M. Rose et al. 2021; J.-P. Beaulieu & E. Bachelet 2021). §2 gives an overview of our data and methods. We present the resulting transformations in §3, and use them to make predictions for the tip of the red giant branch in *JWST*, *Roman*, and *Euclid* filters. We consider optimal filter combinations for various stellar populations applications in §4, and discuss conclusions and future work in §5.

2. DATA AND METHODS

Our input datasets and synthetic photometry technique are described in detail by M. J. Durbin et al. (2023). In this section we provide a brief summary of the process, and discuss minor updates where applicable.

2.1. Data

We combine data products from four spectral libraries to maximize coverage of the full HR diagram at the relevant wavelengths. These are the HST flux standard library CALSPEC (D. A. Turnshek et al. 1990; R. C. Bohlin et al. 2001; R. C. Bohlin 2007; R. C. Bohlin & M. Cohen 2008; R. C. Bohlin et al. 2014; R. C. Bohlin & S. E. Deustua 2019, and references therein); the NASA Infrared Telescope Facility original and extended libraries (IRTF and EIRTF respectively, J. T. Rayner et al. 2009 and A. Villaume et al. 2017); and the X-Shooter Spectral Library third data release (XSL, Y.-P. Chen et al. 2014; A. Gonneau et al. 2020; K. Verro et al. 2022a).

We deredden all library spectra with line-of-sight reddnings adopted from the 3D dust map of R. Lallemand et al. (2022, updated by J. L. Vergely et al. 2022) for Galactic stars, with the majority of distances from C. A. L. Bailer-Jones et al. (2021). For the small subset of library stars that are Magellanic Cloud members, we use the 2D reddening map of D. M. Skowron et al. (2021).

Throughputs for *HST*, 2MASS, and *Roman*/WFI are available via the *HST* calibration reference data system (CRDS)⁶ under the context `hst_synphot_0067 imap`. *JWST* throughputs are described by and available through the *JWST* User Documentation.⁷ The *Euclid*/NISP filter curves are described by Euclid Collab-

oration et al. (2022) and available at the *Euclid* Mission Reference Data website.⁸ (Note that we adopt only the detector-averaged *JWST*/NIRCam filter curves and do not take into account chip-dependent throughput differences, nor do we account for variations in filter cut-off wavelengths over the *Euclid*/NISP and *Roman*/WFI fields of view.) The OGLE-IV *I* filter, a close approximation of the standard Cousins *I*, is described by A. Udalski et al. (2015) and available on the OGLE project website,⁹ and the CTIO/DECam filters are described by T. M. C. Abbott et al. (2018) and available via NOIRLab.¹⁰

Our choice of CTIO/DECam to represent ground-based *izY* is largely based on the slightly redder cutoff of its *i*-band blue edge relative to comparable instruments ($\sim 0.71 \mu\text{m}$ on DECam as opposed to $\sim 0.69 \mu\text{m}$ on SDSS, Pan-STARRS, and Rubin). As the EIRTF library's blue cutoff is $0.7 \mu\text{m}$, the DECam *i*-band allows us to compute higher fidelity synthetic photometry for these spectra. Transformations between DECam and other facilities may be found in T. M. C. Abbott et al. (2021, Appendix B).

On a similar note, we could equally have chosen the F814W filter on WFC3/UVIS as opposed to ACS/WFC, but the ACS/WFC one is more widely used, especially for the distance-scale applications that motivated this work. Differences between these respective filters are generally within ± 0.02 mag, as detailed in S. E. Deustua & J. Mack (2018).

Finally, we note that *JWST* calibration continues to evolve as more in-flight data becomes available (e.g. M. L. Boyer et al. 2022; J. R. Rigby et al. 2023; Z. Ma et al. 2024), and the same is expected for *Euclid* and *Roman* as the missions mature.

2.2. Synthetic photometry

For a spectrum of flux density \mathbf{f}_λ integrated over a set of bandpasses \mathbf{P} sampled on the same wavelength grid, the integrated flux densities \mathbf{f}_P are simply:

$$\mathbf{f}_P = \mathbf{P} \cdot \mathbf{f}_\lambda \quad (1)$$

and the covariance between them is:

$$\text{Cov}[\mathbf{f}_P] = \mathbf{P} \cdot \text{Cov}[\mathbf{f}_\lambda] \cdot \mathbf{P}^T \quad (2)$$

as in Gaia Collaboration et al. (2022) and M. J. Durbin et al. (2023). Individual output magnitudes and uncertainties are available upon request.

⁸ <https://doi.org/10.5270/esa-kx8w57c>

⁹ <https://ogle.astrouw.edu.pl/main/OGLEIV/mosaic.html>

¹⁰ <https://noirlab.edu/science/programs/ctio/filters/Dark-Energy-Camera>

⁶ <https://hst-crds.stsci.edu/>

⁷ <https://jwst-docs.stsci.edu/jwst-near-infrared-camera/nircam-instrumentation/nircam-filters>

Band	Pivot [μm]	AB–Vega [mag]	ST–Vega [mag]	Sirius–Vega [mag]
<i>Euclid</i> /NISP				
Y_E	1.079	0.694	2.166	0.027
J_E	1.362	1.058	3.037	0.023
H_E	1.765	1.493	4.034	0.014
CTIO/DECam, OGLE IV, 2MASS				
i	0.781	0.418	1.190	0.055
I	0.790	0.441	1.237	0.054
z	0.917	0.527	1.647	0.030
Y	0.990	0.582	1.867	0.025
J	1.239	0.913	2.687	0.026
H	1.649	1.391	3.786	0.015
K_S	2.164	1.864	4.848	0.011
<i>HST</i> ACS/WFC + WFC3/IR				
F814W	0.805	0.431	1.267	0.050
F110W	1.153	0.777	2.394	0.026
F125W	1.249	0.920	2.710	0.026
F160W	1.537	1.274	3.515	0.019
<i>JWST</i> /NIRCam				
F090W	0.903	1.821	1.608	0.034
F115W	1.154	2.015	2.413	0.027
F150W	1.501	2.126	3.419	0.020
F200W	1.988	2.422	4.500	0.011
<i>Roman</i> /WFII				
F087	0.870	0.497	1.501	0.040
F106	1.057	0.664	2.091	0.027
F129	1.290	0.972	2.833	0.025
F158	1.575	1.305	3.599	0.018
F184	1.839	1.571	4.203	0.012
F213	2.123	1.826	4.768	0.011

Table 1. Pivot wavelengths and conversions from Vega magnitudes to the AB, ST, and Sirius-Vega systems for all filters. These conversion factors should be added to the Vega magnitudes reported here to obtain transformations and photometry in the desired system.

We use the CALSPEC file `alpha_lyr_stis_011.fits` to calculate our fiducial Vega zeropoints for all bands. We also provide conversions to the ABmag and STmag

systems in Table 1 for convenience, and to the Sirius-Vega system used for *JWST* (G. H. Rieke et al. 2022) as well. Note that for NIRCam, AB magnitudes are redefined to depend solely on pixel area, such that all NIRCam short-wavelength channel filters have nearly the same AB zeropoint; thus, their AB-Vega conversions differ substantially from those for other instruments. All other AB zeropoints are calculated using the traditional definition (J. B. Oke 1974).

3. RESULTS

3.1. Transformation coefficients

We fit continuous piecewise linear transformations using the Python library `pwlfit` (C. F. Jekel & G. Venter 2019), which take the form

$$Y = \begin{cases} c_0 + c_1(X - X_1) & X_1 \leq X \leq X_2 \\ c_0 + c_1(X - X_1) + c_2(X - X_2) & X_2 < X \leq X_3 \\ \vdots & \vdots \\ \sum_{i=1}^n c_{i-1} + c_i(X - X_i) & X_n < X \leq X_{n+1} \end{cases} \quad (3)$$

for a filter pair difference Y , color term X , and number of line segments n .

In M. J. Durbin et al. (2023) we chose the number of line segments for each filter combination visually. In this work, we find the best-fit number of line segments with Bayesian optimization using the `GPyOpt` library (The GPyOpt authors 2016), following the example in the `pwlfit` documentation.¹¹ We set the regularization parameter l to the minimum uncertainty on Y , and impose the additional constraints that all segments must span at least 0.1 mag in color and have at least 25 stars in their color range. In addition to the global rejection criteria described in M. J. Durbin et al. (2023) Section 4.1 (items 2–5), we require stars to have total (random + systematic) uncertainties less than 0.05 mag in the three unique filters used in a given transformation.

We list all transformation coefficients in Tables 2 through 4, and show figures of all fits in Appendix A.

Table 2. Transformations to the *Euclid*/NISP filter system.

Y	X	X_0	X_1	c_0	c_1	σ_{seg}	N_\star	σ_{fit}
From CTIO/DECam + 2MASS								
$Y_E - Y$	$i - Y$		-0.35	-0.02	0.000	-0.125	0.013	34
			-0.02	0.14	-0.007	-0.585	0.015	153

Continued on next page

¹¹ https://jekel.me/piecewise_linear_fit_py/examples.html#find-the-best-number-of-line-segments

Y	X	X_0	X_1	c_0	c_1	σ_{seg}	N_*	σ_{fit}
$Y_E - J$	$J - H$	0.14	1.08	-0.055	-0.253	0.012	418	0.013
		-0.13	0.21	-0.001	0.663	0.012	163	0.013
		0.21	1.03	0.051	0.422	0.013	598	0.013
	$J - K_S$	-0.29	-0.03	-0.008	0.287	0.010	30	0.013
		-0.03	0.25	0.001	0.596	0.016	142	0.013
		0.25	1.35	0.067	0.330	0.012	589	0.013
$J_E - J$	$J - H$	-0.13	0.35	-0.007	-0.340	0.007	339	0.007
		0.35	1.03	-0.029	-0.279	0.007	441	0.007
		-0.29	-0.00	-0.007	-0.166	0.007	38	0.009
	$J - K_S$	-0.00	0.28	-0.007	-0.311	0.010	164	0.009
		0.28	0.71	-0.026	-0.246	0.009	435	0.009
		0.71	1.35	-0.080	-0.170	0.011	143	0.009
$H_E - H$	$J - H$	-0.13	-0.03	-0.006	-0.266	0.009	28	0.013
		-0.03	0.42	-0.001	-0.045	0.013	368	0.013
		0.42	1.03	0.026	-0.107	0.013	382	0.013
From <i>HST</i> WFC3/IR								
$Y_E - \text{F110W}$	F110W–F160W	-0.17	0.09	0.003	0.117	0.003	70	0.006
		0.09	1.09	-0.003	0.187	0.006	691	0.006
		-0.09	0.15	-0.003	0.858	0.011	138	0.015
$Y_E - \text{F125W}$	F125W–F160W	0.15	0.54	0.037	0.596	0.015	571	0.015
		0.54	0.76	-0.053	0.762	0.025	52	0.015
		-0.17	0.26	0.001	-0.635	0.006	160	0.006
$J_E - \text{F110W}$	F110W–F160W	0.26	1.09	-0.022	-0.547	0.007	613	0.006
		-0.09	0.76	-0.004	-0.396	0.004	778	0.004
		-0.56	0.06	0.004	0.106	0.009	48	0.011
$J_E - \text{F160W}$	F814W–F160W	0.06	1.43	-0.003	0.219	0.010	510	0.011
		1.43	2.29	0.105	0.143	0.021	48	0.011
		-0.17	0.26	0.001	0.364	0.005	159	0.006
	F110W–F160W	0.26	1.09	-0.022	0.453	0.007	614	0.006
		-0.09	0.76	-0.004	0.604	0.004	778	0.004
		-0.56	0.69	0.006	-0.099	0.012	233	0.015
	F125W–F160W	0.69	2.29	0.058	-0.174	0.016	372	0.015
		-0.17	-0.00	-0.002	-0.426	0.011	37	0.015
		-0.00	0.32	-0.001	-0.135	0.009	165	0.015
	F110W–F160W	0.32	0.68	0.067	-0.351	0.016	446	0.015
		0.68	1.09	0.160	-0.487	0.021	124	0.015
		-0.09	0.26	0.016	-0.316	0.013	283	0.018
$F125W - F160W$	F115W–F160W	0.26	0.50	0.058	-0.480	0.019	391	0.018
		0.50	0.76	0.162	-0.687	0.025	102	0.018
		-0.27	0.01	-0.003	-0.307	0.008	39	0.009
From <i>JWST</i> /NIRCam								
$Y_E - \text{F115W}$	F115W–F150W	-0.13	0.19	-0.006	0.299	0.006	127	0.007
		0.19	0.68	0.008	0.229	0.006	588	0.007
		0.68	0.96	-0.072	0.346	0.011	46	0.007
$F115W - F200W$	F115W–F200W	-0.27	0.33	0.003	0.196	0.007	180	0.007
		0.33	1.53	0.021	0.141	0.006	579	0.007
		-0.13	0.27	-0.000	-0.644	0.003	186	0.004
$J_E - \text{F115W}$	F115W–F150W	0.27	0.96	-0.013	-0.595	0.005	588	0.004
		-0.27	0.01	-0.003	-0.307	0.008	39	0.009

Continued on next page

Y	X	X_0	X_1	c_0	c_1	σ_{seg}	N_*	σ_{fit}
J_E –F150W	F090W–F150W	0.01	0.32	-0.001	-0.513	0.010	130	0.009
		0.32	0.82	-0.046	-0.370	0.009	432	0.009
		0.82	1.53	-0.102	-0.301	0.010	170	0.009
	F115W–F150W	-0.38	0.15	0.009	0.146	0.006	75	0.008
		0.15	1.64	-0.003	0.220	0.009	551	0.008
	F150W–F200W	-0.13	0.27	-0.000	0.356	0.003	186	0.004
		0.27	0.96	-0.014	0.406	0.005	588	0.004
		-0.17	-0.03	0.004	0.343	0.008	28	0.018
		-0.03	0.08	0.022	0.959	0.018	183	0.018
H_E –F150W	F090W–F150W	0.08	0.23	0.046	0.673	0.016	336	0.018
		0.23	0.57	0.101	0.429	0.021	253	0.018
		-0.38	0.49	0.009	-0.164	0.010	176	0.015
	F115W–F150W	0.49	1.64	0.068	-0.283	0.016	449	0.015
		-0.13	0.01	0.008	-0.561	0.012	37	0.015
		0.01	0.26	0.003	-0.237	0.010	149	0.015
	F150W–F200W	0.26	0.60	0.071	-0.493	0.015	457	0.015
		0.60	0.96	0.178	-0.672	0.019	129	0.015
		-0.17	0.57	-0.011	-0.744	0.010	815	0.010
H_E –F200W	F090W–F200W	-0.51	-0.12	0.006	0.134	0.010	30	0.012
		-0.12	1.02	-0.005	0.039	0.012	352	0.012
		1.02	2.14	-0.053	0.085	0.012	242	0.012
	F115W–F200W	-0.27	-0.05	0.001	0.242	0.008	27	0.011
		-0.05	0.77	-0.009	0.067	0.011	533	0.011
		0.77	1.53	-0.072	0.149	0.013	211	0.011
	F150W–F200W	-0.17	-0.03	0.004	0.484	0.006	27	0.009
		-0.03	0.25	-0.004	0.209	0.009	574	0.009
		0.25	0.57	-0.029	0.311	0.009	214	0.009

Table 3. Transformations to the *JWST*/NIRCam filter system.

Y	X	X_0	X_1	c_0	c_1	σ_{seg}	N_*	σ_{fit}
From <i>Euclid</i> /NISP								
$F115W$ – Y_E	Y_E – H_E	-0.25	0.34	0.001	-0.181	0.005	156	0.006
		0.34	1.63	-0.014	-0.136	0.006	604	0.006
$F115W$ – J_E	J_E – H_E	-0.13	0.85	0.003	-0.292	0.005	761	0.005
		-0.12	0.01	0.004	0.655	0.010	37	0.013
$F150W$ – J_E	J_E – H_E	0.01	0.15	0.002	1.119	0.015	137	0.013
		0.15	0.41	0.067	0.671	0.012	412	0.013
	Y_E – J_E	0.41	0.78	0.116	0.551	0.012	186	0.013
		-0.13	0.85	0.003	0.708	0.005	761	0.005
$F150W$ – H_E	J_E – H_E	-0.12	0.26	-0.011	-0.516	0.006	368	0.008
		0.26	0.78	-0.039	-0.411	0.009	433	0.008
	Y_E – J_E	-0.13	0.21	-0.002	-0.380	0.006	160	0.008
		0.21	0.85	0.020	-0.481	0.009	601	0.008
$F150W$ – H_E	J_E – H_E	-0.12	0.26	-0.011	0.484	0.006	368	0.008
		0.26	0.78	-0.039	0.590	0.009	433	0.008
	Y_E – H_E	-0.25	0.55	-0.016	0.209	0.009	317	0.011
		0.55	1.63	-0.074	0.315	0.012	443	0.011

Continued on next page

Y	X	X_0	X_1	c_0	c_1	σ_{seg}	N_*	σ_{fit}
F200W– H_E	J_E-H_E	−0.12	0.47	0.013	−0.153	0.013	686	0.013
		0.47	0.78	0.083	−0.301	0.016	114	0.013
	Y_E-H_E	−0.25	−0.05	−0.003	−0.269	0.011	29	0.012
		−0.05	0.82	0.007	−0.056	0.011	485	0.012
		0.82	1.63	0.078	−0.143	0.013	245	0.012
		From CTIO/DECam, OGLE IV, 2MASS						
F090W– i	$i-Y$	−0.35	−0.03	0.001	−0.551	0.004	34	0.007
		−0.03	1.08	−0.001	−0.643	0.007	571	0.007
	$i-z$	−0.23	0.78	−0.008	−0.892	0.003	605	0.003
		−0.02	0.62	0.002	−0.123	0.011	126	0.015
	$I-K_S$	−0.80	−0.02	−0.001	−0.320	0.017	37	0.015
		0.62	1.51	0.024	−0.158	0.011	353	0.015
		1.51	2.79	0.113	−0.217	0.026	96	0.015
F090W– z	$i-z$	−0.23	0.78	−0.008	0.108	0.003	605	0.003
F090W– Y	$i-Y$	−0.35	−0.04	0.003	0.453	0.004	33	0.007
		−0.04	1.08	−0.001	0.357	0.007	572	0.007
F115W– J	$J-H$	−0.13	0.22	0.002	0.348	0.006	171	0.006
		0.22	1.03	0.030	0.219	0.006	603	0.006
	$J-K_S$	−0.29	0.42	0.011	0.247	0.008	349	0.007
		0.42	1.35	0.049	0.158	0.006	425	0.007
F150W– H	$J-H$	−0.13	0.35	−0.011	0.283	0.009	337	0.010
		0.35	1.03	−0.045	0.379	0.010	443	0.010
F200W– K_S	$I-K_S$	−0.80	2.79	−0.010	0.017	0.017	610	0.017
		−0.29	0.23	−0.012	0.085	0.013	160	0.017
	$J-K_S$	0.23	0.70	0.005	0.009	0.017	471	0.017
		0.70	1.35	−0.045	0.080	0.018	146	0.017
		From HST ACS/WFC + WFC3/IR						
F090W–F814W	F814W–F160W	−0.56	0.01	0.007	−0.293	0.012	41	0.012
		0.01	0.57	0.005	−0.142	0.009	126	0.012
		0.57	1.29	0.027	−0.179	0.009	351	0.012
		1.29	2.29	0.173	−0.293	0.024	88	0.012
F115W–F110W	F110W–F160W	−0.17	0.17	0.008	−0.114	0.005	107	0.005
		0.17	1.09	−0.007	−0.023	0.005	665	0.005
F115W–F125W	F125W–F160W	−0.09	0.16	0.001	0.455	0.006	142	0.009
		0.16	0.76	0.021	0.326	0.009	632	0.009
F150W–F160W	F814W–F160W	−0.56	−0.03	−0.005	0.007	0.004	35	0.005
		−0.03	2.29	−0.004	0.045	0.005	571	0.005
	F110W–F160W	−0.17	1.09	−0.004	0.087	0.005	773	0.005
		−0.09	0.76	−0.004	0.124	0.004	778	0.004

Table 4. Transformations to the *Roman*/WFI filter system.

Y	X	X_0	X_1	c_0	c_1	σ_{seg}	N_*	σ_{fit}
From <i>Euclid</i> /NISP								
F106– Y_E	Y_E-H_E	−0.25	1.63	0.000	0.046	0.003	759	0.003
		−0.13	0.85	−0.002	0.092	0.003	760	0.003
F129– J_E	J_E-H_E	−0.12	0.26	0.007	0.275	0.004	367	0.005
		0.26	0.78	0.025	0.205	0.005	415	0.005

Continued on next page

Y	X	X_0	X_1	c_0	c_1	σ_{seg}	N_\star	σ_{fit}
From CTIO/DECam, OGLE IV, 2MASS								
F087- J_E	Y_E-J_E	-0.13	0.16	0.002	0.197	0.003	119	0.004
		0.16	0.85	-0.006	0.244	0.005	642	0.004
	J_E-H_E	-0.12	0.26	-0.007	-0.694	0.007	368	0.009
		0.26	0.78	-0.025	-0.624	0.010	433	0.009
F158- H_E	Y_E-J_E	-0.13	0.24	0.004	-0.502	0.009	182	0.012
		0.24	0.85	0.054	-0.712	0.013	579	0.012
	J_E-H_E	-0.12	0.26	-0.007	0.308	0.007	367	0.009
		0.26	0.78	-0.025	0.377	0.010	434	0.009
F184- H_E	Y_E-H_E	-0.25	0.55	-0.010	0.133	0.009	320	0.010
		0.55	1.63	-0.048	0.201	0.011	440	0.010
	J_E-H_E	-0.12	-0.02	-0.008	-0.323	0.006	29	0.009
		-0.02	0.18	-0.003	-0.026	0.007	185	0.009
F106- Y	Y_E-H_E	0.18	0.78	0.017	-0.133	0.010	585	0.009
		-0.25	-0.02	-0.006	-0.156	0.007	30	0.009
	$i-Y$	-0.02	0.46	-0.003	-0.011	0.007	197	0.009
		0.46	1.63	0.024	-0.071	0.010	531	0.009
From <i>HST</i> ACS/WFC + WFC3/IR								
F087-F814W	F814W-F160W	-0.56	-0.03	0.006	-0.185	0.008	35	0.009
		-0.03	1.25	0.008	-0.118	0.006	470	0.009
	F160W-F213Ks	1.25	2.29	0.114	-0.203	0.016	101	0.009
		-0.80	2.79	-0.001	0.005	0.004	612	0.004
F213-Ks	$I-K_S$	-0.29	1.35	-0.001	0.010	0.004	780	0.004
		-0.80	2.79	-0.001	0.005	0.004	612	0.004

Continued on next page

Y	X	X_0	X_1	c_0	c_1	σ_{seg}	N_*	σ_{fit}
F106–F110W	F110W–F160W	−0.17	0.74	0.003	0.242	0.007	699	0.007
		0.74	1.09	−0.070	0.340	0.011	61	0.007
F106–F125W	F125W–F160W	−0.09	0.14	−0.005	1.000	0.013	131	0.018
		0.14	0.54	0.039	0.683	0.017	576	0.018
		0.54	0.76	−0.085	0.912	0.031	53	0.018
F129–F110W	F110W–F160W	−0.17	0.22	0.003	−0.487	0.006	135	0.008
		0.22	1.09	−0.024	−0.367	0.008	638	0.008
F129–F125W	F125W–F160W	−0.09	0.76	−0.003	−0.146	0.003	778	0.003
F158–F160W	F814W–F160W	−0.56	0.77	0.003	−0.013	0.002	277	0.003
		0.77	2.29	0.022	−0.037	0.004	329	0.003
	F110W–F160W	−0.17	0.46	0.004	−0.029	0.003	375	0.004
		0.46	1.09	0.033	−0.092	0.006	398	0.004
	F125W–F160W	−0.09	0.32	0.004	−0.044	0.003	379	0.005
		0.32	0.76	0.029	−0.123	0.006	399	0.005
From <i>JWST/NIRCam</i>								
F087–F090W	F090W–F150W	−0.38	−0.00	−0.006	0.141	0.006	38	0.005
		−0.00	0.91	−0.007	0.060	0.004	413	0.005
		0.91	1.64	−0.049	0.106	0.007	169	0.005
	F090W–F200W	−0.51	−0.01	−0.005	0.103	0.006	38	0.005
		−0.01	1.28	−0.006	0.048	0.004	472	0.005
		1.28	2.14	−0.045	0.078	0.009	108	0.005
F106–F090W	F090W–F150W	−0.38	0.03	0.016	−0.480	0.014	45	0.012
		0.03	0.75	0.008	−0.236	0.011	296	0.012
		0.75	1.64	0.072	−0.321	0.013	285	0.012
	F090W–F200W	−0.51	0.06	0.014	−0.355	0.016	48	0.014
		0.06	0.90	0.003	−0.187	0.012	284	0.014
		0.90	2.14	0.035	−0.223	0.015	292	0.014
F106–F115W	F115W–F150W	−0.13	0.18	−0.008	0.397	0.009	123	0.009
		0.18	0.68	0.010	0.299	0.009	589	0.009
		0.68	0.96	−0.111	0.476	0.016	48	0.009
	F115W–F200W	−0.27	0.32	0.003	0.257	0.010	170	0.009
		0.32	1.53	0.025	0.187	0.009	588	0.009
F129–F115W	F115W–F150W	−0.13	0.25	0.000	−0.454	0.004	175	0.007
		0.25	0.96	−0.016	−0.389	0.007	599	0.007
	F115W–F200W	−0.27	0.01	−0.002	−0.223	0.006	39	0.008
		0.01	0.32	−0.001	−0.357	0.008	129	0.008
		0.32	0.83	−0.037	−0.242	0.007	442	0.008
		0.83	1.53	−0.077	−0.195	0.009	161	0.008
F129–F150W	F090W–F150W	−0.38	0.07	0.009	0.201	0.009	51	0.012
		0.07	1.64	−0.001	0.334	0.012	575	0.012
	F115W–F150W	−0.13	0.25	0.000	0.546	0.004	175	0.007
		0.25	0.96	−0.016	0.611	0.007	599	0.007
	F150W–F200W	−0.17	−0.03	−0.001	0.449	0.012	27	0.027
		−0.03	0.07	0.033	1.525	0.028	153	0.027
		0.07	0.22	0.068	1.047	0.025	334	0.027
		0.22	0.57	0.153	0.653	0.031	267	0.027
F158–F150W	F090W–F150W	−0.38	0.41	0.003	−0.051	0.004	144	0.005
		0.41	1.64	0.024	−0.102	0.005	482	0.005

Continued on next page

Y	X	X_0	X_1	c_0	c_1	σ_{seg}	N_*	σ_{fit}
F184–F200W	F115W–F150W	-0.13	0.38	0.007	-0.123	0.005	351	0.005
		0.38	0.96	0.040	-0.209	0.006	423	0.005
	F150W–F200W	-0.17	0.57	-0.005	-0.266	0.007	815	0.007
F213–F200W	F090W–F200W	-0.51	2.14	-0.008	0.019	0.009	623	0.009
	F115W–F200W	-0.27	0.10	-0.007	0.086	0.007	72	0.008
F213–F200W		0.10	0.85	-0.001	0.016	0.008	554	0.008
		0.85	1.53	-0.047	0.070	0.009	144	0.008
	F150W–F200W	-0.17	0.06	-0.006	0.179	0.006	153	0.008
		0.06	0.28	0.003	0.035	0.008	519	0.008
		0.28	0.57	-0.029	0.151	0.009	142	0.008
F213–F200W	F090W–F200W	-0.51	0.38	0.010	-0.033	0.011	122	0.015
		0.38	2.14	-0.001	-0.005	0.016	502	0.015
	F115W–F200W	-0.27	0.30	0.010	-0.061	0.012	161	0.015
		0.30	0.83	-0.010	0.007	0.015	449	0.015
	F150W–F200W	-0.17	0.07	0.004	-0.184	0.014	167	0.015
		0.07	0.27	-0.009	0.021	0.015	487	0.015
		0.27	0.57	0.027	-0.116	0.016	161	0.015

3.2. Predictions for the tip of the red giant branch

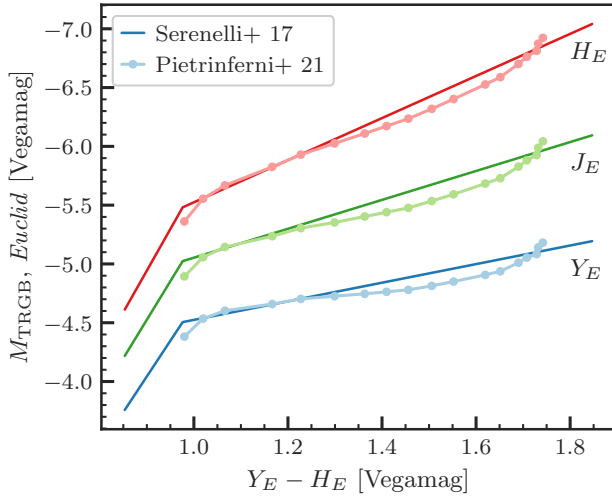


Figure 2. *Euclid*/NISP Y_E , J_E , and H_E TRGB magnitudes as a function of $Y_E - H_E$ color for the A. Serenelli et al. (2017) and A. Pietrinferni et al. (2021) theoretical TRGB calibrations.

As a demonstration of how these transformations may be used, we convert theoretical predictions of the tip of the red giant branch absolute magnitude from ground-based and WFC3/IR bandpasses into the *JWST*, *Roman*, and *Euclid* systems. The tip of the red giant branch (TRGB) is the terminal point of a low-mass ($\lesssim 2 M_\odot$) star’s first ascent of the red giant branch, when core helium ignition halts the expansion and cooling of

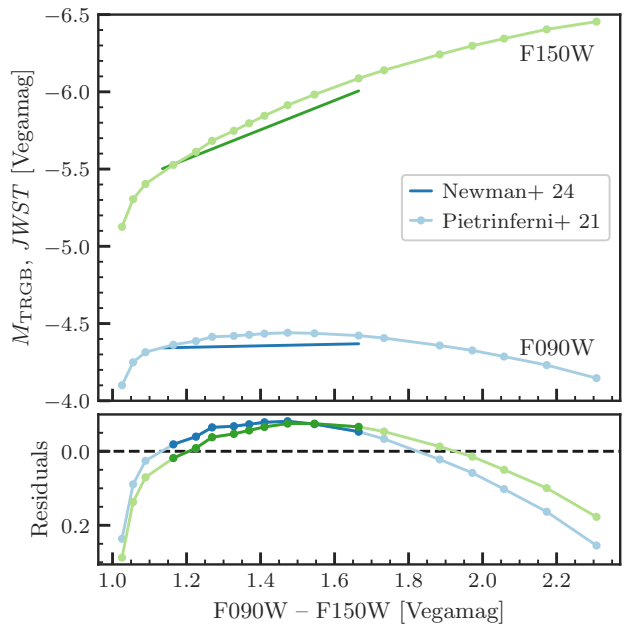


Figure 3. *JWST*/NIRCam F090W and F150W TRGB magnitudes as a function of F090W – F150W color for the A. Pietrinferni et al. (2021) theoretical and M. J. B. Newman et al. (2024a) empirical TRGB calibrations, with residuals in the lower panel.

its atmosphere (M. Salaris & S. Cassisi 2006). This produces a well-defined edge in color-magnitude space, which enables the TRGB to be used to great effect as a distance indicator in the local universe (e.g. M. G. Lee et al. 1993; R. L. Beaton et al. 2018; W. L. Freedman et al. 2019; G. S. Anand et al. 2024). *JWST* has already

Stellar parameters ^a			<i>Euclid</i>			<i>JWST</i>				<i>Roman</i>			
[Fe/H]	$\log L/L_{\odot}$	$\log T_{\text{eff}}$	Y_E	J_E	H_E	F090W	F115W	F150W	F200W	F087	F129	F158	F213
-3.20	3.180	3.651	-4.38	-4.89	-5.36	-4.10	-4.53	-5.13	-5.40	-4.04	-4.77	-5.21	-5.41
-2.50	3.239	3.646	-4.54	-5.06	-5.55	-4.25	-4.68	-5.30	-5.58	-4.19	-4.93	-5.40	-5.59
-2.20	3.264	3.637	-4.60	-5.14	-5.67	-4.31	-4.76	-5.40	-5.70	-4.25	-5.02	-5.50	-5.71
-1.90	3.288	3.623	-4.66	-5.24	-5.83	-4.36	-4.83	-5.53	-5.85	-4.29	-5.10	-5.64	-5.86
-1.70	3.305	3.612	-4.70	-5.30	-5.93	-4.39	-4.88	-5.61	-5.96	-4.31	-5.16	-5.73	-5.97
-1.55	3.317	3.603	-4.73	-5.35	-6.03	-4.41	-4.91	-5.68	-6.05	-4.33	-5.21	-5.81	-6.06
-1.40	3.329	3.592	-4.75	-5.40	-6.11	-4.42	-4.94	-5.75	-6.14	-4.32	-5.25	-5.88	-6.16
-1.30	3.337	3.585	-4.76	-5.44	-6.17	-4.43	-4.96	-5.80	-6.21	-4.33	-5.28	-5.93	-6.23
-1.20	3.345	3.577	-4.78	-5.48	-6.24	-4.43	-4.99	-5.85	-6.28	-4.33	-5.32	-5.99	-6.30
-1.05	3.357	3.566	-4.81	-5.54	-6.32	-4.44	-5.03	-5.91	-6.38	-4.33	-5.37	-6.06	-6.40
-0.90	3.369	3.555	-4.85	-5.59	-6.40	-4.44	-5.07	-5.98	-6.47	-4.31	-5.42	-6.13	-6.49
-0.70	3.385	3.537	-4.91	-5.68	-6.53	-4.42	-5.14	-6.09	-6.61	-4.28	-5.51	-6.25	-6.64
-0.60	3.392	3.528	-4.94	-5.73	-6.59	-4.41	-5.18	-6.14	-6.68	-4.26	-5.55	-6.30	-6.71
-0.40	3.404	3.511	-5.01	-5.83	-6.70	-4.36	-5.26	-6.24	-6.82	-4.20	-5.64	-6.41	-6.85
-0.30	3.410	3.501	-5.05	-5.88	-6.76	-4.33	-5.31	-6.30	-6.88	-4.16	-5.69	-6.47	-6.92
-0.20	3.414	3.492	-5.08	-5.93	-6.81	-4.29	-5.34	-6.34	-6.95	-4.11	-5.73	-6.51	-6.98
-0.08	3.417	3.481	-5.14	-5.99	-6.87	-4.23	-5.40	-6.40	-7.02	-4.04	-5.79	-6.57	-7.05
0.06	3.418	3.468	-5.18	-6.04	-6.92	-4.15	-5.45	-6.45	-7.10	-3.94	-5.85	-6.62	-7.13

^aReproduced from A. Pietrinferni et al. (2021) Table 4.

Table 5. TRGB absolute magnitudes in *Euclid*, *JWST*, and *Roman* bands for BaSTI α -enhanced 12.5 Gyr isochrones as a function of metallicity, transformed from *IJKH* magnitudes originally reported in A. Pietrinferni et al. (2021). All magnitudes are in the Vega system.

made TRGB detections out to 30 Mpc (T. Carleton et al. 2024). With significantly smaller apertures, *Euclid* and *Roman* may not have the depth of *JWST*, but they will deliver unprecedented spatial coverage of any and all Local Volume galaxies within their footprints, providing robust statistical samples of the ancient, metal-poor, dust-free halo populations where the TRGB is most effective as a distance indicator (R. L. Beaton et al. 2018, 2019).

We choose two recent theoretical calibrations of the TRGB to translate to *Euclid*, *JWST*, and *Roman* bands. While a plethora of empirical calibrations in the relevant bands exist as well (e.g. E. Valenti et al. 2004; J. J. Dalcanton et al. 2012; M. Górski et al. 2018; T. J. Hoyt et al. 2018; M. A. T. Groenewegen et al. 2019; M. J. Durbin et al. 2020; M. J. B. Newman et al. 2024b), we prefer these theoretical predictions for their larger dynamic ranges in color (metallicity). A. Serenelli et al. (2017) establish a set of concordance physics for the TRGB with two stellar model suites and predict its color-absolute magnitude relations in the *VI*, J_{KS} , and F110W, F160W bands. A. Pietrinferni et al. (2021) provide absolute *IJKH* magnitudes for a 12.5 Gyr α -enhanced TRGB as a function of metallicity with the BaSTI model suite.

We present transformed magnitudes for the BaSTI TRGB in Table 5, and transformed color-magnitude relations from A. Serenelli et al. (2017) in Table 6. For *Euclid* we use $Y_E - H_E$ as the color baseline throughout, as all *Euclid* pointings will include all three NISP filters. For *JWST* and *Roman* we convert the A. Serenelli et al. (2017) J_{KS} relations to F115W, F200W and F129, F213 respectively, and the F110W, F160W relations to F106, F158.

In Figure 3 we compare the BaSTI F090W, F150W TRGB to the recent empirical calibration of M. J. B. Newman et al. (2024a), which we convert from Sirius-Vega to Vega magnitudes using the coefficients in Table 1. The mean residuals over the valid color range of the empirical relation ($1.14 < F090W - F150W < 1.67$ in Vega mags, corresponding to $-1.9 \leq [\text{Fe}/\text{H}] \leq -0.7$ in the BaSTI models) are -0.06 and -0.05 mag for F090W and F150W respectively, in the theoretical – empirical direction.

4. DISCUSSION

The majority of our filter transformations require two or three components (49 and 28 filter combinations respectively), and the remainder require one or four (17 and 11). As in M. J. Durbin et al. (2023), the most consistent sources of slope changes are the Paschen jump, which occurs at $0.82 \mu\text{m}$ and peaks in A-type stars (B. J.

<i>Euclid</i>			
$M_{Y_E}^{\text{TRGB}}$	$= \begin{cases} -4.51 - 6.07[(Y_E - H_E) - 0.98] \\ -4.51 - 0.79[(Y_E - H_E) - 0.98] \end{cases}$	$0.85 < Y_E - H_E < 0.98$	$0.98 \leq Y_E - H_E < 1.62$
$M_{J_E}^{\text{TRGB}}$	$= \begin{cases} -5.02 - 6.55[(Y_E - H_E) - 0.98] \\ -5.02 - 1.23[(Y_E - H_E) - 0.98] \end{cases}$	$0.85 < Y_E - H_E < 0.98$	$0.98 \leq Y_E - H_E < 1.62$
$M_{H_E}^{\text{TRGB}}$	$= \begin{cases} -5.48 - 7.07[(Y_E - H_E) - 0.98] \\ -5.48 - 1.79[(Y_E - H_E) - 0.98] \end{cases}$	$0.85 < Y_E - H_E < 0.98$	$0.98 \leq Y_E - H_E < 1.62$
<i>JWST</i>			
$M_{\text{F115W}}^{\text{TRGB}}$	$= \begin{cases} -4.80 - 1.41[(\text{F115W} - \text{F200W}) - 0.91] + 25.78[(\text{F115W} - \text{F200W}) - 0.91]^2 \\ -4.80 - 0.61[(\text{F115W} - \text{F200W}) - 0.91] - 0.45[(\text{F115W} - \text{F200W}) - 0.91]^2 \end{cases}$	$0.73 < \text{F115W} - \text{F200W} < 0.91$	$0.91 \leq \text{F115W} - \text{F200W} < 1.71$
$M_{\text{F200W}}^{\text{TRGB}}$	$= \begin{cases} -5.71 - 2.41[(\text{F115W} - \text{F200W}) - 0.91] + 25.78[(\text{F115W} - \text{F200W}) - 0.91]^2 \\ -5.71 - 1.61[(\text{F115W} - \text{F200W}) - 0.91] - 0.45[(\text{F115W} - \text{F200W}) - 0.91]^2 \end{cases}$	$0.73 < \text{F115W} - \text{F200W} < 0.91$	$0.91 \leq \text{F115W} - \text{F200W} < 1.71$
<i>Roman</i>			
$M_{\text{F106}}^{\text{TRGB}}$	$= \begin{cases} -4.47 - 6.96[(\text{F106} - \text{F158}) - 0.88] \\ -4.47 - 0.82[(\text{F106} - \text{F158}) - 0.88] \end{cases}$	$0.77 < \text{F106} - \text{F158} < 0.88$	$0.88 \leq \text{F106} - \text{F158} < 1.85$
$M_{\text{F158}}^{\text{TRGB}}$	$= \begin{cases} -5.34 - 7.96[(\text{F106} - \text{F158}) - 0.88] \\ -5.34 - 1.82[(\text{F106} - \text{F158}) - 0.88] \end{cases}$	$0.77 < \text{F106} - \text{F158} < 0.88$	$0.88 \leq \text{F106} - \text{F158} < 1.85$
$M_{\text{F129}}^{\text{TRGB}}$	$= \begin{cases} -5.04 - 1.12[(\text{F129} - \text{F213}) - 0.67] + 44.95[(\text{F129} - \text{F213}) - 0.67]^2 \\ -5.04 - 0.94[(\text{F129} - \text{F213}) - 0.67] - 0.60[(\text{F129} - \text{F213}) - 0.67]^2 \end{cases}$	$0.52 < \text{F129} - \text{F213} < 0.67$	$0.67 \leq \text{F129} - \text{F213} < 1.35$
$M_{\text{F213}}^{\text{TRGB}}$	$= \begin{cases} -5.71 - 2.12[(\text{F129} - \text{F213}) - 0.67] + 44.95[(\text{F129} - \text{F213}) - 0.67]^2 \\ -5.71 - 1.94[(\text{F129} - \text{F213}) - 0.67] - 0.60[(\text{F129} - \text{F213}) - 0.67]^2 \end{cases}$	$0.52 < \text{F129} - \text{F213} < 0.67$	$0.67 \leq \text{F129} - \text{F213} < 1.35$

Table 6. Predicted color-absolute magnitude relations for the TRGB in *Euclid*, *JWST*, and *Roman* bands based on $J - K_S$ and F110W–F160W relations from A. Serenelli et al. (2017).

Taylor 1986; V. Straizys 1998), and the 1.65 μm bump, where the dominant source of H $^{-}$ continuum opacity transitions from bound-free to free-free absorption, most prominently in M stars (T. L. John 1988; J. T. Rayner et al. 2009; C. Allende Prieto 2023).

The most closely analogous filters (e.g., the synthetic magnitudes are within ± 0.1 mag across the full color range of our data) include: F090W and z ; F106 and Y_E ; F115W and F110W; F150W, F158, and F160W; and F200W, F213, and K_S .

Euclid Collaboration et al. (2022) provide transformations between NISP and several ground-based NIR instruments for models of O through K type stars, MLT stars, and galaxies. Their $H_E - H_{2\text{MASS}}$ vs. $J - H$ relation for O-K stars (their eqn. C.20) is the one most directly comparable to ours. The slope of the reddest segment of ours, -0.107 , is in good agreement with theirs, -0.12 , which is dominated by redder stars. However, our zeropoints differ by 0.05 mag when put onto the same magnitude system, and their color range is less than half of ours.

A. Sanghi et al. (2023) and A. Sanghi et al. (2024) derive absolute magnitude-spectral type relations for ultracool MLT-type dwarf stars in *JWST*, *Roman*, and *Euclid* filters using the low-resolution IRTF/SpeX prism spectral libraries (A. J. Burgasser 2014). Although there

is little if any overlap between the respective samples and spectral type coverage, when taken together these papers and ours are highly complementary, spanning ~ 30 absolute magnitudes in the NIR.

In Figure 4 we show distributions of the average transformation residuals for several subtypes of evolved stars, all of which are frequently used in distance scale work. For Cepheids, RR Lyrae, and RGB stars, the 16th and 84th percentile residuals are all within ± 0.01 mag, but for O-rich AGB stars they are -0.08 , $+0.10$, and ± 0.06 for C-rich AGB stars. Note that for RGB stars these residual dispersions may or may not directly translate to uncertainties on the TRGB, as we have few upper RGB stars and none at extreme low or high metallicities, where the TRGB slope is least certain (P.-F. Wu et al. 2014; A. Serenelli et al. 2017). Similarly, the residual dispersions of the AGB stars do not necessarily indicate fundamental systematics on distance measurements made with them, only that cross-calibrating said measurements must be done in a more bespoke manner than with simple color-dependent transformations.

5. CONCLUSIONS

We have presented transformations between NIR broadband filters on *JWST*, *Roman*, *Euclid*, *HST*, and several ground-based instruments. We have additionally applied these transformations to predict color-

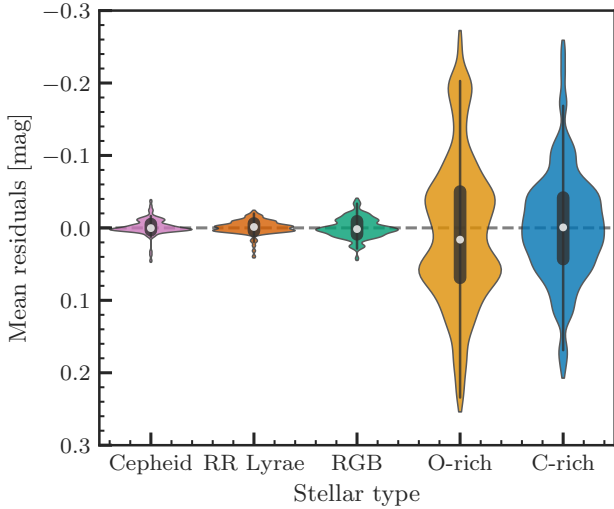


Figure 4. Distributions of average transformation residuals for Cepheids, RR Lyrae, RGB stars, and O- and C-rich AGB stars.

magnitude relations for the theoretical tip of the red giant branch as seen with *JWST*, *Roman*, and *Euclid*.

In future, a comparison with state-of-the-art stellar atmosphere models such as the recently updated BOSZ library (R. C. Bohlin et al. 2017; S. Mészáros et al. 2024) would be illuminating, both as a diagnostic of overall agreement between models and observations, and as a way to directly examine the effects of stellar physics and atmospheric composition—particularly carbon and other α -element abundances—on broadband NIR fluxes.

A similar study of filter transforms for integrated light, such as with the XSL simple stellar population models (K. Vero et al. 2022b), would be of interest as well for unresolved populations.

ACKNOWLEDGMENTS

Support for this work was provided by NASA through HST program GO-15875. Support for this work was provided by the NSF through NSF grant AST-2108616.

This research has made use of the SVO Filter Profile Service (<http://svo2.cab.inta-csic.es/theory/fps/>) supported from the Spanish MINECO through grant AYA2017-84089.

This publication makes use of data products from the Two Micron All Sky Survey, which is a joint project of the University of Massachusetts and the Infrared Processing and Analysis Center/California Institute of Technology, funded by the National Aeronautics and Space Administration and the National Science Foundation.

This work has made use of data from the European Space Agency (ESA) mission *Gaia* (<https://www.cosmos.esa.int/gaia>), processed by the *Gaia* Data Processing and Analysis Consortium (DPAC, <https://www.cosmos.esa.int/web/gaia/dpac/consortium>). Funding for the DPAC has been provided by national institutions, in particular the institutions participating in the *Gaia* Multilateral Agreement.

This research has made use of NASA’s Astrophysics Data System.

This research has made use of the SIMBAD database, operated at CDS, Strasbourg, France. The original description of the SIMBAD service was published in M. Wenger et al. (2000).

This research has made use of the VizieR catalogue access tool, CDS, Strasbourg, France (DOI: 10.26093/cds/vizier). The original description of the VizieR service was published in F. Ochsenbein et al. (2000).

This research made use of the cross-match service provided by CDS, Strasbourg.

This research has used data, tools or materials developed as part of the EXPLORE project that has received funding from the European Union’s Horizon 2020 research and innovation programme under grant agreement No 101004214.

Facilities: CDS, MAST, IRTF, XShooter, HST:STIS, HST:NICMOS, HST:WFC3/IR

Software: Astropy (Astropy Collaboration et al. 2013, 2018), Astroquery (A. Ginsburg et al. 2017, 2019), Dust_extinction (K. Gordon et al. 2022), Dustmaps (G. Green 2018), Matplotlib (J. D. Hunter 2007), NumPy (S. van der Walt et al. 2011; C. R. Harris et al. 2020), Pandas (W. McKinney 2010, 2011), pwlf (C. F. Jekel & G. Venter 2019), PyVO (M. Graham et al. 2014), Seaborn (M. Waskom 2021), SciPy (P. Virtanen et al. 2020), Specutils (N. Earl et al. 2022), Stsynphot (STScI Development Team 2020), Synphot (STScI Development Team 2018)

REFERENCES

Abbott, T. M. C., Abdalla, F. B., Allam, S., et al. 2018,

ApJS, 239, 18, doi: [10.3847/1538-4365/aae9f0](https://doi.org/10.3847/1538-4365/aae9f0)

Abbott, T. M. C., Adamów, M., Aguena, M., et al. 2021,

ApJS, 255, 20, doi: [10.3847/1538-4365/ac00b3](https://doi.org/10.3847/1538-4365/ac00b3)

- Akeson, R., Armus, L., Bachelet, E., et al. 2019, arXiv e-prints, arXiv:1902.05569.
<https://arxiv.org/abs/1902.05569>
- Allende Prieto, C. 2023, Atoms, 11, 61, doi: 10.3390/atoms11030061
- Anand, G. S., Riess, A. G., Yuan, W., et al. 2024, ApJ, 966, 89, doi: 10.3847/1538-4357/ad2e0a
- Astropy Collaboration, Robitaille, T. P., Tollerud, E. J., et al. 2013, A&A, 558, A33, doi: 10.1051/0004-6361/201322068
- Astropy Collaboration, Price-Whelan, A. M., Sipőcz, B. M., et al. 2018, AJ, 156, 123, doi: 10.3847/1538-3881/aabc4f
- Bailer-Jones, C. A. L., Rybizki, J., Fouesneau, M., Demleitner, M., & Andrae, R. 2021, AJ, 161, 147, doi: 10.3847/1538-3881/abd806
- Beaton, R. L., Bono, G., Braga, V. F., et al. 2018, SSRv, 214, 113, doi: 10.1007/s11214-018-0542-1
- Beaton, R. L., Seibert, M., Hatt, D., et al. 2019, ApJ, 885, 141, doi: 10.3847/1538-4357/ab4263
- Beaulieu, J.-P., & Bachelet, E. 2021, in European Planetary Science Congress, EPSC2021–298, doi: 10.5194/epsc2021-298
- Bohlin, R. C. 2007, in Astronomical Society of the Pacific Conference Series, Vol. 364, The Future of Photometric, Spectrophotometric and Polarimetric Standardization, ed. C. Sterken, 315, doi: 10.48550/arXiv.astro-ph/0608715
- Bohlin, R. C., & Cohen, M. 2008, AJ, 136, 1171, doi: 10.1088/0004-6256/136/3/1171
- Bohlin, R. C., & Deustua, S. E. 2019, AJ, 157, 229, doi: 10.3847/1538-3881/ab1b50
- Bohlin, R. C., Dickinson, M. E., & Calzetti, D. 2001, AJ, 122, 2118, doi: 10.1086/323137
- Bohlin, R. C., Gordon, K. D., & Tremblay, P. E. 2014, PASP, 126, 711, doi: 10.1086/677655
- Bohlin, R. C., Mészáros, S., Fleming, S. W., et al. 2017, AJ, 153, 234, doi: 10.3847/1538-3881/aa6ba9
- Boyer, M. L., Anderson, J., Gennaro, M., et al. 2022, Research Notes of the American Astronomical Society, 6, 191, doi: 10.3847/2515-5172/ac923a
- Burgasser, A. J. 2014, in Astronomical Society of India Conference Series, Vol. 11, Astronomical Society of India Conference Series, 7–16, doi: 10.48550/arXiv.1406.4887
- Carleton, T., Ellsworth-Bowers, T., Windhorst, R. A., et al. 2024, ApJL, 961, L37, doi: 10.3847/2041-8213/ad1b56
- Chary, R., Helou, G., Brammer, G., et al. 2020, arXiv e-prints, arXiv:2008.10663, doi: 10.48550/arXiv.2008.10663
- Chen, Y.-P., Trager, S. C., Peletier, R. F., et al. 2014, A&A, 565, A117, doi: 10.1051/0004-6361/201322505
- Dalcanton, J. J., Williams, B. F., Melbourne, J. L., et al. 2012, ApJS, 198, 6, doi: 10.1088/0067-0049/198/1/6
- Deustua, S. E., & Mack, J. 2018,, Instrument Science Report WFC3 2018-02, 33 pages
- Durbin, M. J., Beaton, R. L., Dalcanton, J. J., Williams, B. F., & Boyer, M. L. 2020, ApJ, 898, 57, doi: 10.3847/1538-4357/ab9cbb
- Durbin, M. J., Beaton, R. L., Monson, A. J., Swidler, B., & Dalcanton, J. J. 2023, AJ, 166, 236, doi: 10.3847/1538-3881/acfaa1
- Earl, N., Tollerud, E., Jones, C., et al. 2022,, v1.7.0 Zenodo, doi: 10.5281/zenodo.6207491
- Euclid Collaboration, Schirmer, M., Jahnke, K., et al. 2022, A&A, 662, A92, doi: 10.1051/0004-6361/202142897
- Euclid Collaboration et al. 2024, arXiv e-prints, arXiv:2405.13491, doi: 10.48550/arXiv.2405.13491
- Freedman, W. L., Madore, B. F., Hatt, D., et al. 2019, ApJ, 882, 34, doi: 10.3847/1538-4357/ab2f73
- Gaia Collaboration, Montegriffo, P., Bellazzini, M., et al. 2022, arXiv e-prints, arXiv:2206.06215, doi: 10.48550/arXiv.2206.06215
- Ginsburg, A., Parikh, M., Woillez, J., et al. 2017, <http://ascl.net/1708.004>
- Ginsburg, A., Sipőcz, B. M., Brasseur, C. E., et al. 2019, AJ, 157, 98, doi: 10.3847/1538-3881/aafc33
- Gonneau, A., Lyubenova, M., Lançon, A., et al. 2020, A&A, 634, A133, doi: 10.1051/0004-6361/201936825
- Gordon, K., Larson, K., McBride, A., et al. 2022,, v1.1 GitHub. https://github.com/karllark/dust_extinction/releases/tag/v1.1
- Górski, M., Pietrzyński, G., Gieren, W., et al. 2018, AJ, 156, 278, doi: 10.3847/1538-3881/aaeacb
- Graham, M., Plante, R., Tody, D., & Fitzpatrick, M. 2014, <http://ascl.net/1402.004>
- Green, G. 2018, The Journal of Open Source Software, 3, 695, doi: 10.21105/joss.00695
- Groenewegen, M. A. T., Cioni, M. R. L., Girardi, L., et al. 2019, A&A, 622, A63, doi: 10.1051/0004-6361/201833904
- Harris, C. R., Millman, K. J., van der Walt, S. J., et al. 2020, Nature, 585, 357, doi: 10.1038/s41586-020-2649-2
- Hoyt, T. J., Freedman, W. L., Madore, B. F., et al. 2018, ApJ, 858, 12, doi: 10.3847/1538-4357/aab7ed
- Hunter, J. D. 2007, Computing in Science and Engineering, 9, 90, doi: 10.1109/MCSE.2007.55
- Jekel, C. F., & Venter, G. 2019, pwlf: A Python Library for Fitting 1D Continuous Piecewise Linear Functions. https://github.com/cjekel/piecewise_linear_fit_py
- John, T. L. 1988, A&A, 193, 189

- Lallement, R., Vergely, J. L., Babusiaux, C., & Cox, N. L. J. 2022, A&A, 661, A147, doi: [10.1051/0004-6361/202142846](https://doi.org/10.1051/0004-6361/202142846)
- Lee, M. G., Freedman, W. L., & Madore, B. F. 1993, ApJ, 417, 553, doi: [10.1086/173334](https://doi.org/10.1086/173334)
- Ma, Z., Yan, H., Sun, B., et al. 2024, PASP, 136, 024501, doi: [10.1088/1538-3873/ad1f3e](https://doi.org/10.1088/1538-3873/ad1f3e)
- McKinney, W. 2010, in Proceedings of the 9th Python in Science Conference, ed. S. van der Walt & Jarrod Millman, Austin, TX, 56–61, doi: [10.25080/Majora-92bf1922-00a](https://doi.org/10.25080/Majora-92bf1922-00a)
- McKinney, W. 2011, Python for High Performance and Scientific Computing, 14. <https://www.semanticscholar.org/paper/pandas%3A-a-Foundational-Python-Library-for-Data-and-McKinney/1a62eb61b2663f8135347171e30cb9dc0a8931b5>
- Mészáros, S., Bohlin, R., Allende Prieto, C., et al. 2024, A&A, 688, A197, doi: [10.1051/0004-6361/202449306](https://doi.org/10.1051/0004-6361/202449306)
- Newman, M. J. B., McQuinn, K. B. W., Skillman, E. D., et al. 2024a, arXiv e-prints, arXiv:2406.03532, doi: [10.48550/arXiv.2406.03532](https://doi.org/10.48550/arXiv.2406.03532)
- Newman, M. J. B., McQuinn, K. B. W., Skillman, E. D., et al. 2024b, ApJ, 966, 175, doi: [10.3847/1538-4357/ad306d](https://doi.org/10.3847/1538-4357/ad306d)
- Ochsenbein, F., Bauer, P., & Marcout, J. 2000, A&AS, 143, 23, doi: [10.1051/aas:2000169](https://doi.org/10.1051/aas:2000169)
- Oke, J. B. 1974, ApJS, 27, 21, doi: [10.1086/190287](https://doi.org/10.1086/190287)
- Pietrinferni, A., Hidalgo, S., Cassisi, S., et al. 2021, ApJ, 908, 102, doi: [10.3847/1538-4357/abd4d5](https://doi.org/10.3847/1538-4357/abd4d5)
- Rayner, J. T., Cushing, M. C., & Vacca, W. D. 2009, ApJS, 185, 289, doi: [10.1088/0067-0049/185/2/289](https://doi.org/10.1088/0067-0049/185/2/289)
- Rieke, G. H., Su, K., Sloan, G. C., & Schlawin, E. 2022, AJ, 163, 45, doi: [10.3847/1538-3881/ac3b5d](https://doi.org/10.3847/1538-3881/ac3b5d)
- Rigby, J., & et al. 2023, PASP, 135, 048001, doi: [10.1088/1538-3873/abc293](https://doi.org/10.1088/1538-3873/abc293)
- Rigby, J. R., Lightsey, P. A., García Marín, M., et al. 2023, PASP, 135, 048002, doi: [10.1088/1538-3873/acbcf4](https://doi.org/10.1088/1538-3873/acbcf4)
- Rose, B. M., Aldering, G., Dai, M., et al. 2021, arXiv e-prints, arXiv:2104.01199, doi: [10.48550/arXiv.2104.01199](https://doi.org/10.48550/arXiv.2104.01199)
- Salaris, M., & Cassisi, S. 2006, Evolution of Stars and Stellar Populations, 1st edn. (Wiley)
- Sanghi, A., Liu, M. C., Best, W. M., et al. 2023, Research Notes of the American Astronomical Society, 7, 194, doi: [10.3847/2515-5172/acf864](https://doi.org/10.3847/2515-5172/acf864)
- Sanghi, A., Liu, M. C., Dupuy, T. J., et al. 2024, Research Notes of the American Astronomical Society, 8, 137, doi: [10.3847/2515-5172/ad4cec](https://doi.org/10.3847/2515-5172/ad4cec)
- Serenelli, A., Weiss, A., Cassisi, S., Salaris, M., & Pietrinferni, A. 2017, A&A, 606, A33, doi: [10.1051/0004-6361/201731004](https://doi.org/10.1051/0004-6361/201731004)
- Skowron, D. M., Skowron, J., Udalski, A., et al. 2021, ApJS, 252, 23, doi: [10.3847/1538-4365/abcb81](https://doi.org/10.3847/1538-4365/abcb81)
- Straizys, V. 1998, Baltic Astronomy, 7, 571, doi: [10.1515/astro-1998-0404](https://doi.org/10.1515/astro-1998-0404)
- STScI Development Team. 2018, <http://ascl.net/1811.001>
- STScI Development Team. 2020, <http://ascl.net/2010.003>
- Taylor, B. J. 1986, ApJS, 60, 577, doi: [10.1086/191098](https://doi.org/10.1086/191098)
- The GPyOpt authors. 2016,, <http://github.com/SheffieldML/GPyOpt>
- Turnshek, D. A., Bohlin, R. C., Williamson, R. L., I., et al. 1990, AJ, 99, 1243, doi: [10.1086/115413](https://doi.org/10.1086/115413)
- Udalski, A., Szymański, M. K., & Szymański, G. 2015, AcA, 65, 1, doi: [10.48550/arXiv.1504.05966](https://doi.org/10.48550/arXiv.1504.05966)
- Valenti, E., Ferraro, F. R., & Origlia, L. 2004, MNRAS, 354, 815, doi: [10.1111/j.1365-2966.2004.08249.x](https://doi.org/10.1111/j.1365-2966.2004.08249.x)
- van der Walt, S., Colbert, S. C., & Varoquaux, G. 2011, Computing in Science & Engineering, 13, 22, doi: [10.1109/MCSE.2011.37](https://doi.org/10.1109/MCSE.2011.37)
- Vergely, J. L., Lallement, R., & Cox, N. L. J. 2022, A&A, 664, A174, doi: [10.1051/0004-6361/202243319](https://doi.org/10.1051/0004-6361/202243319)
- Verro, K., Trager, S. C., Peletier, R. F., et al. 2022a, A&A, 660, A34, doi: [10.1051/0004-6361/202142388](https://doi.org/10.1051/0004-6361/202142388)
- Verro, K., Trager, S. C., Peletier, R. F., et al. 2022b, A&A, 661, A50, doi: [10.1051/0004-6361/202142387](https://doi.org/10.1051/0004-6361/202142387)
- Villaume, A., Conroy, C., Johnson, B., et al. 2017, ApJS, 230, 23, doi: [10.3847/1538-4365/aa72ed](https://doi.org/10.3847/1538-4365/aa72ed)
- Virtanen, P., Gommers, R., Oliphant, T. E., et al. 2020, Nature Methods, 17, 261, doi: [10.1038/s41592-019-0686-2](https://doi.org/10.1038/s41592-019-0686-2)
- Waskom, M. 2021, The Journal of Open Source Software, 6, 3021, doi: [10.21105/joss.03021](https://doi.org/10.21105/joss.03021)
- Wenger, M., Ochsenbein, F., Egret, D., et al. 2000, A&AS, 143, 9, doi: [10.1051/aas:2000332](https://doi.org/10.1051/aas:2000332)
- Wu, P.-F., Tully, R. B., Rizzi, L., et al. 2014, AJ, 148, 7, doi: [10.1088/0004-6256/148/1/7](https://doi.org/10.1088/0004-6256/148/1/7)

APPENDIX

A. FIGURES

Figures 5 through 7 show *JWST* vs. *HST*, DECam *izY* and 2MASS *JHK_S*, and Euclid respectively. Figures 8 through 10 show Euclid vs. *HST*, DECam+2MASS, and *JWST* respectively. Figures 11 through 14 show Roman vs. *HST*, DECam+2MASS, Euclid, and *JWST* respectively.

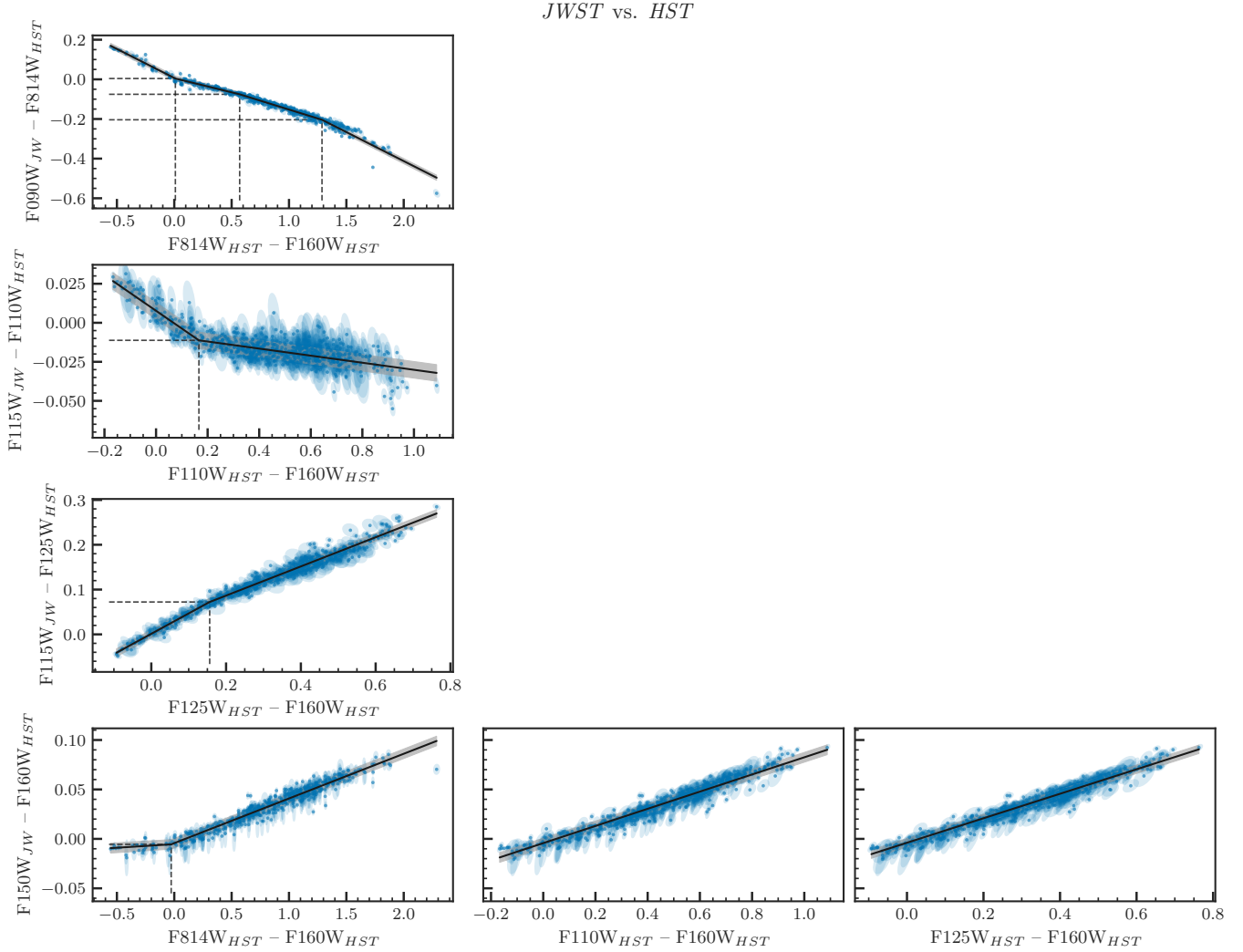


Figure 5. Filter transformations (black lines) for converting HST filters to JWST, with scatter as grey bands, and original data points and errors as blue points and ellipses.

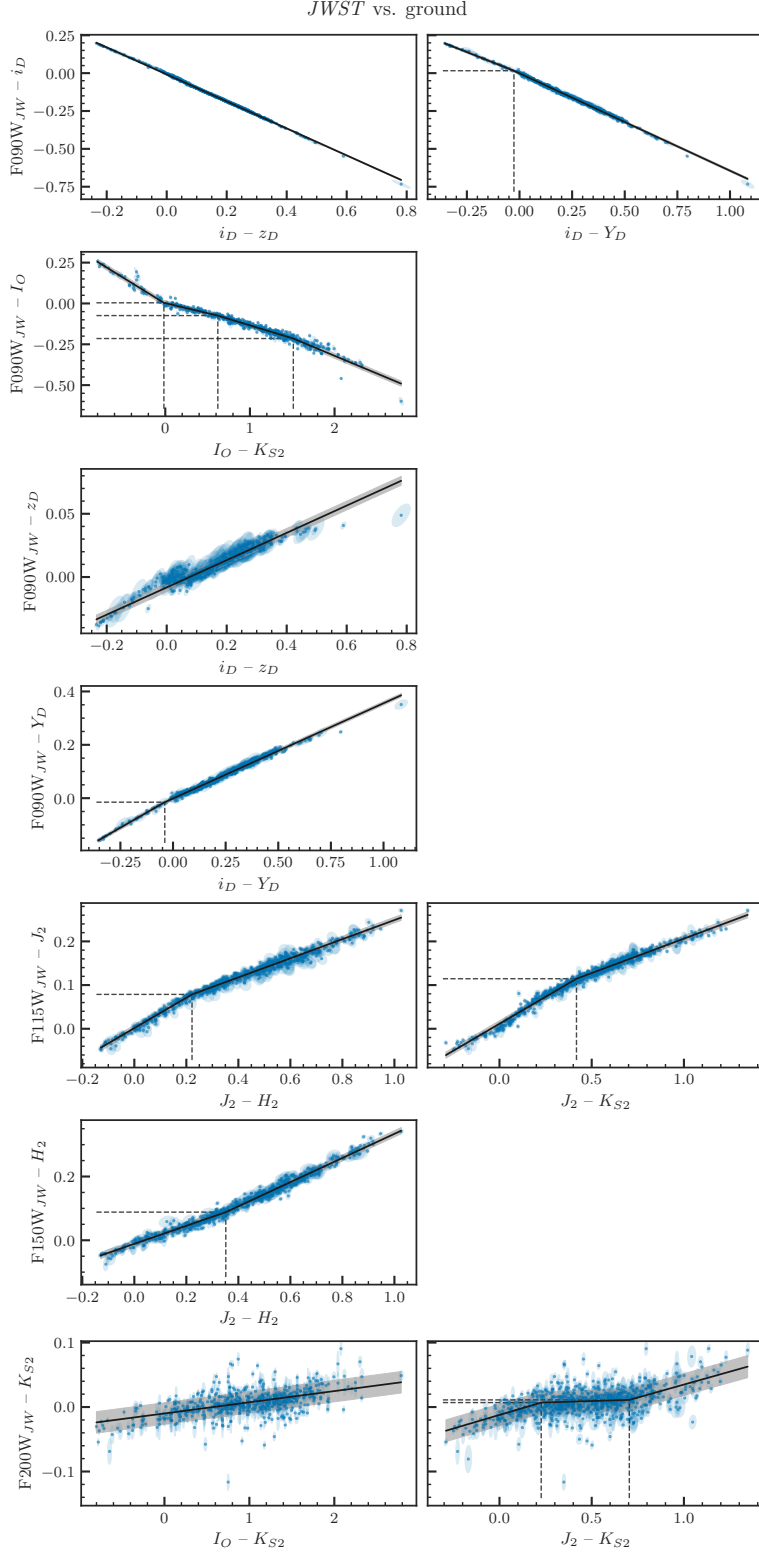


Figure 6. As Figure 5 for converting ground filters to JWST.

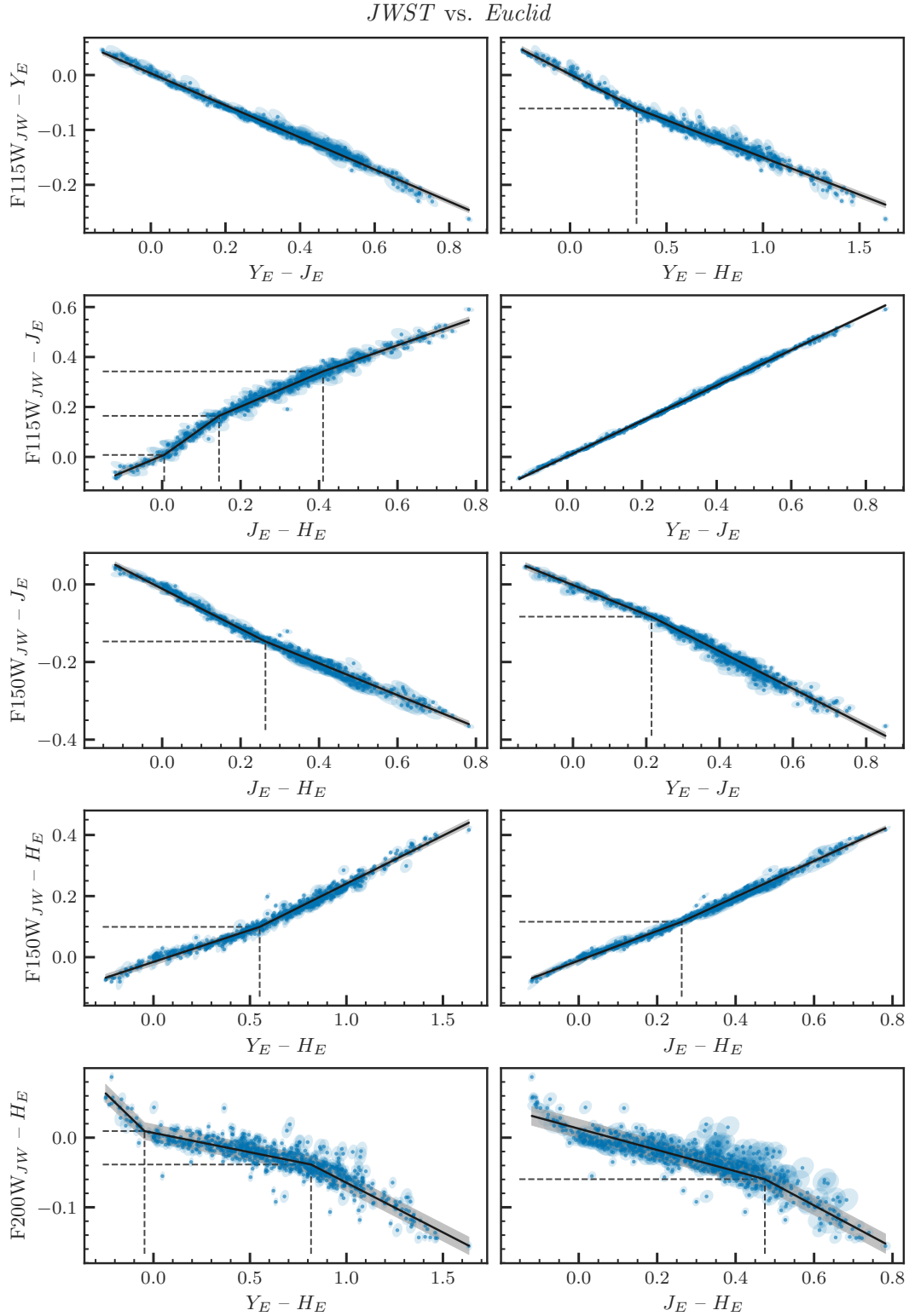
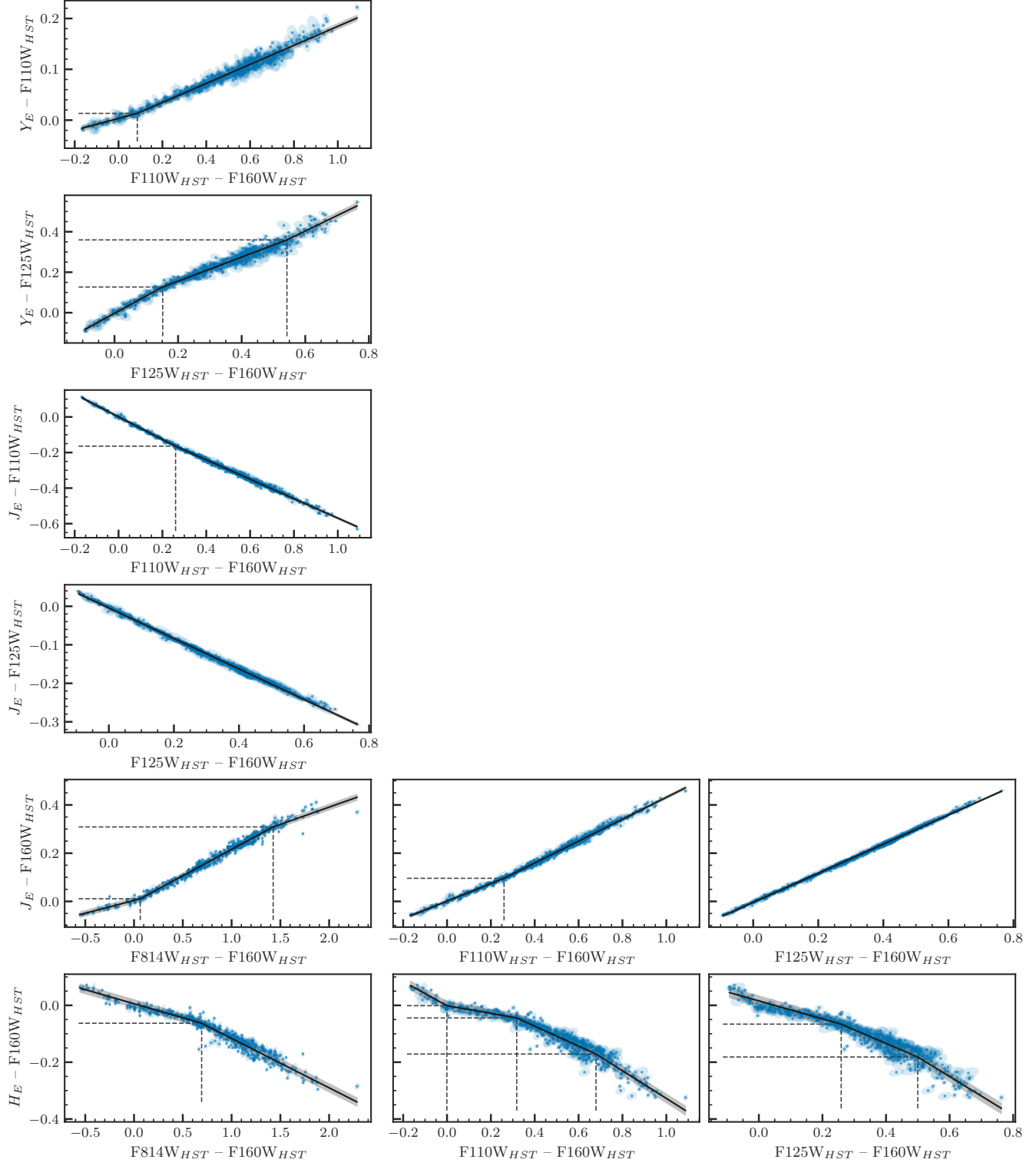


Figure 7. As [Figure 5](#) for converting Euclid filters to JWST.

Euclid vs. HST

**Figure 8.** As Figure 5 for converting HST filters to Euclid.

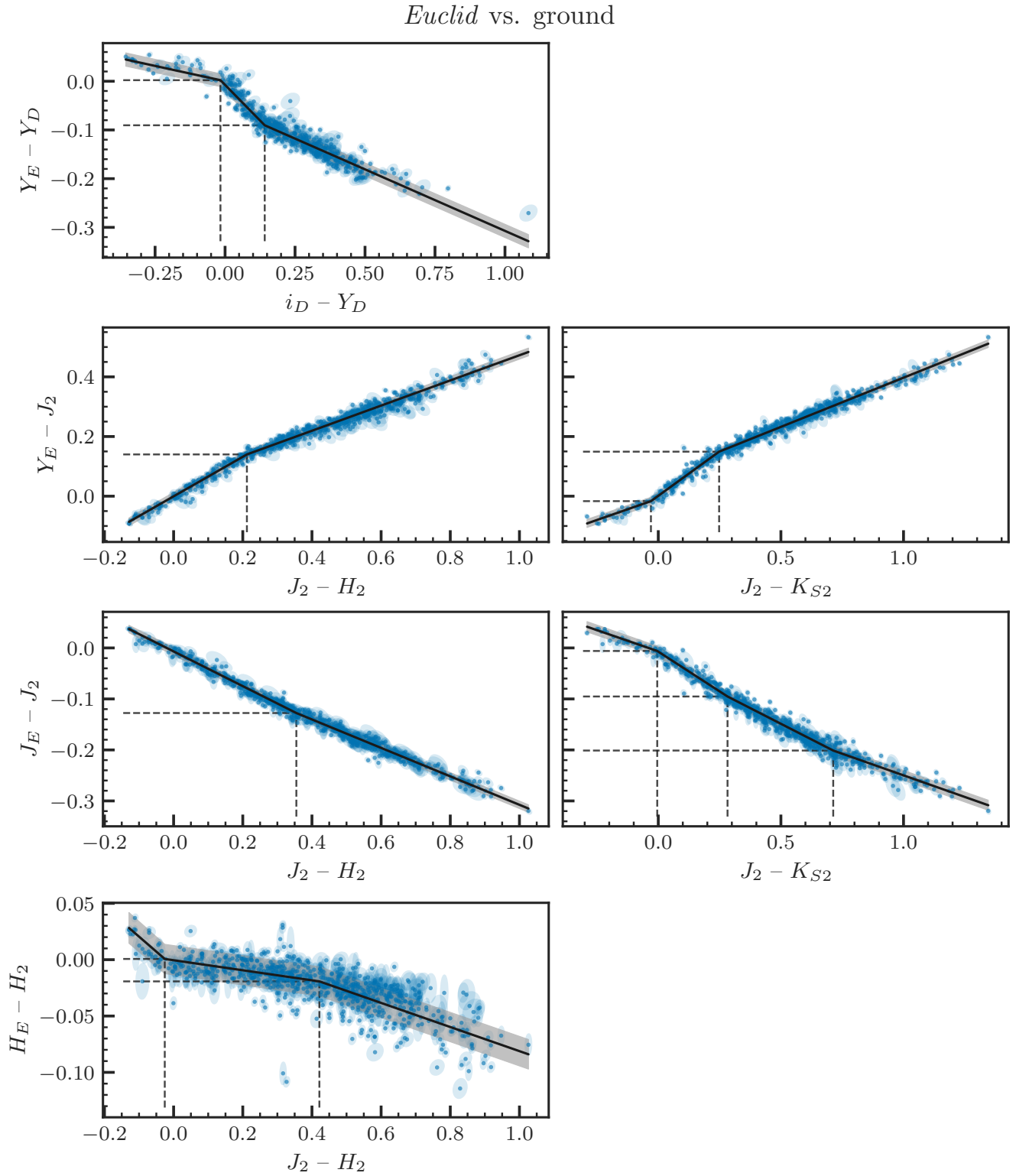


Figure 9. As Figure 5 for converting ground filters to Euclid.

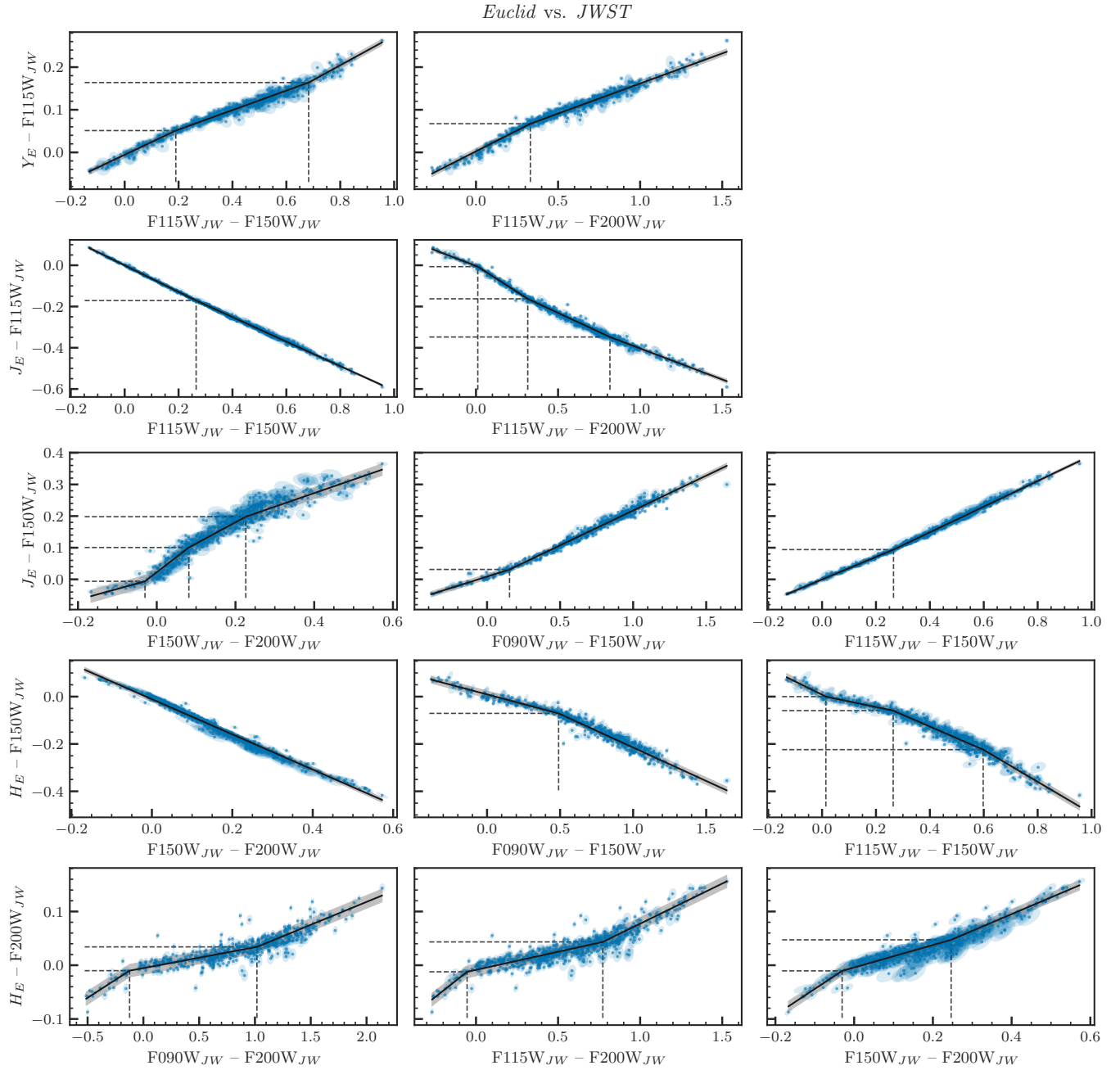
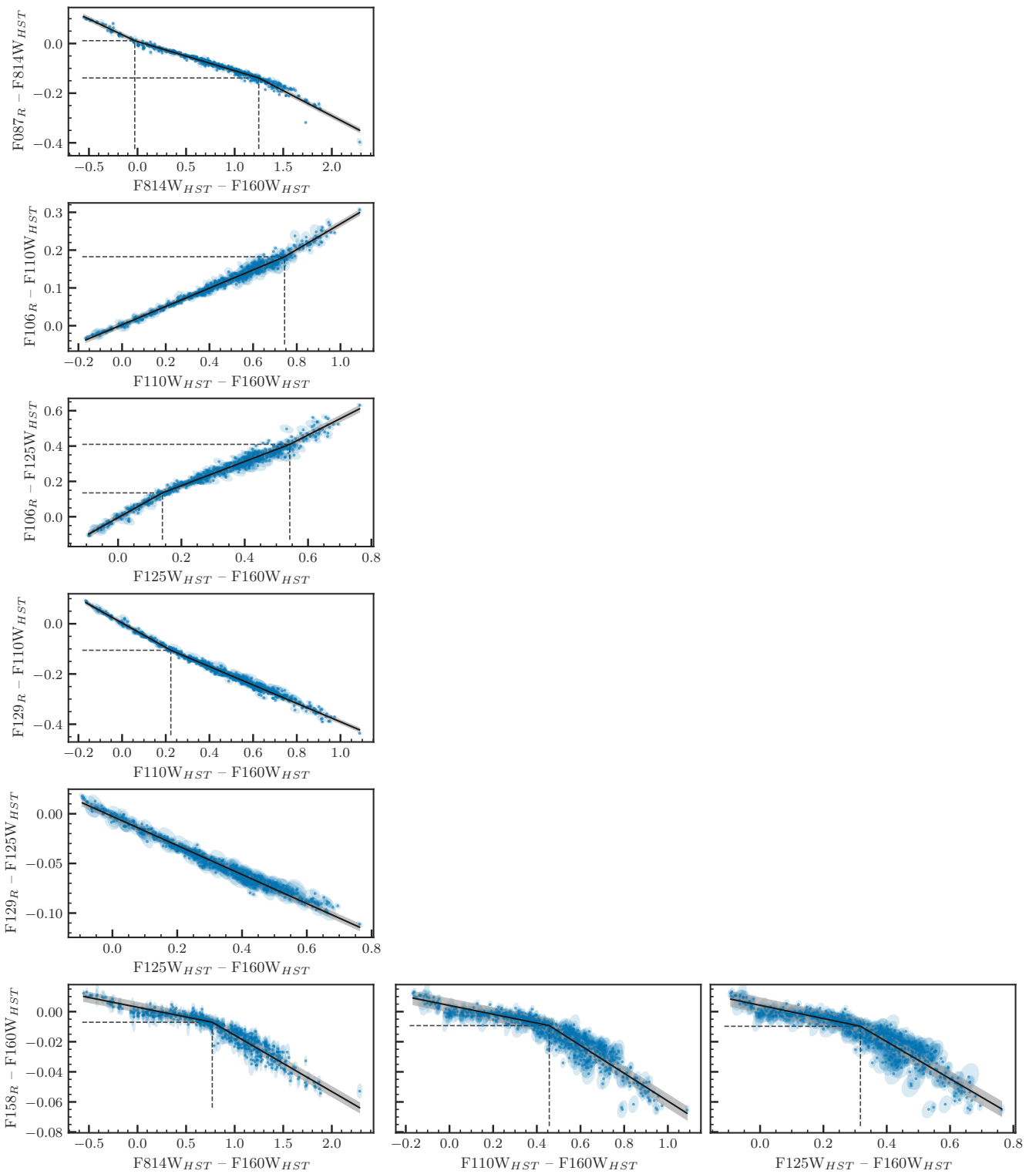


Figure 10. As Figure 5 for converting JWST filters to Euclid.

Roman vs. HST

**Figure 11.** As Figure 5 for converting HST filters to Roman.

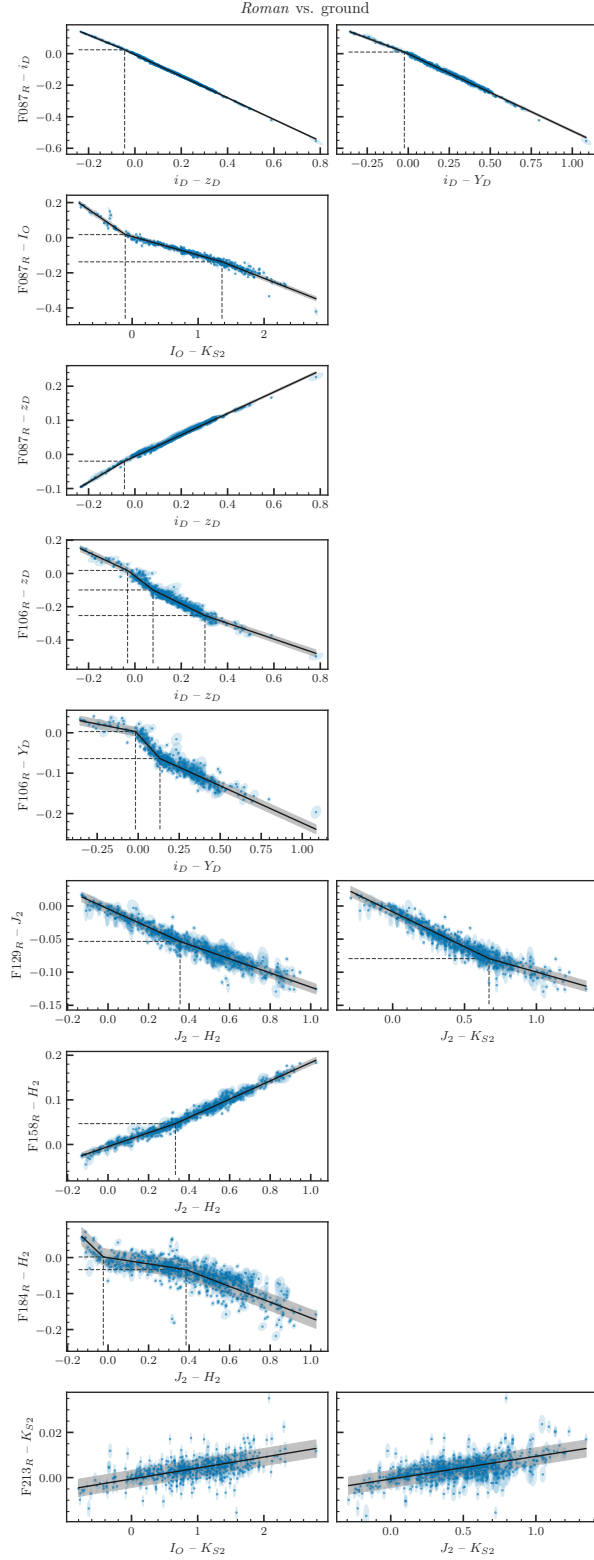


Figure 12. As Figure 5 for converting ground filters to Roman.

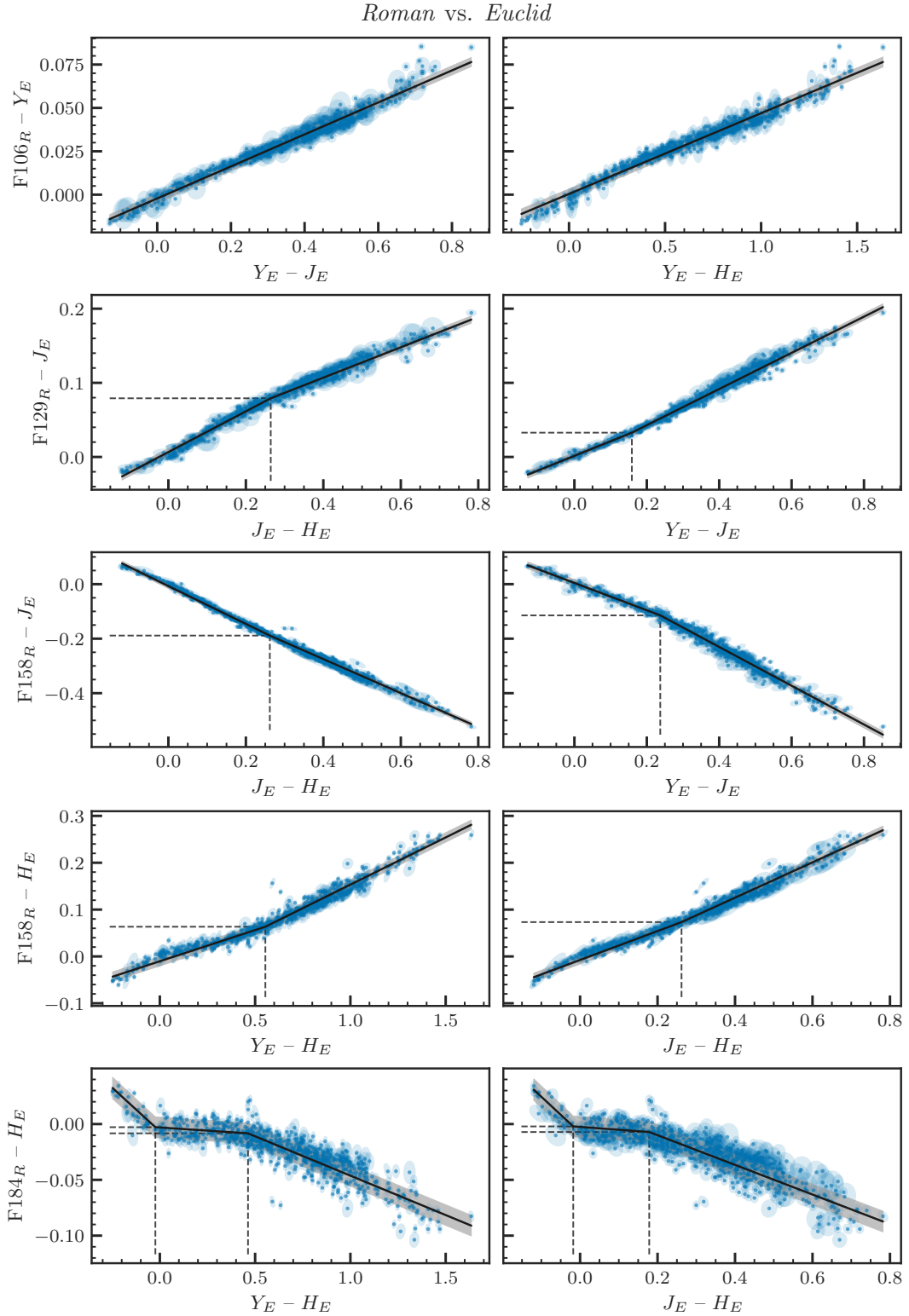


Figure 13. As Figure 5 for converting Euclid filters to Roman.

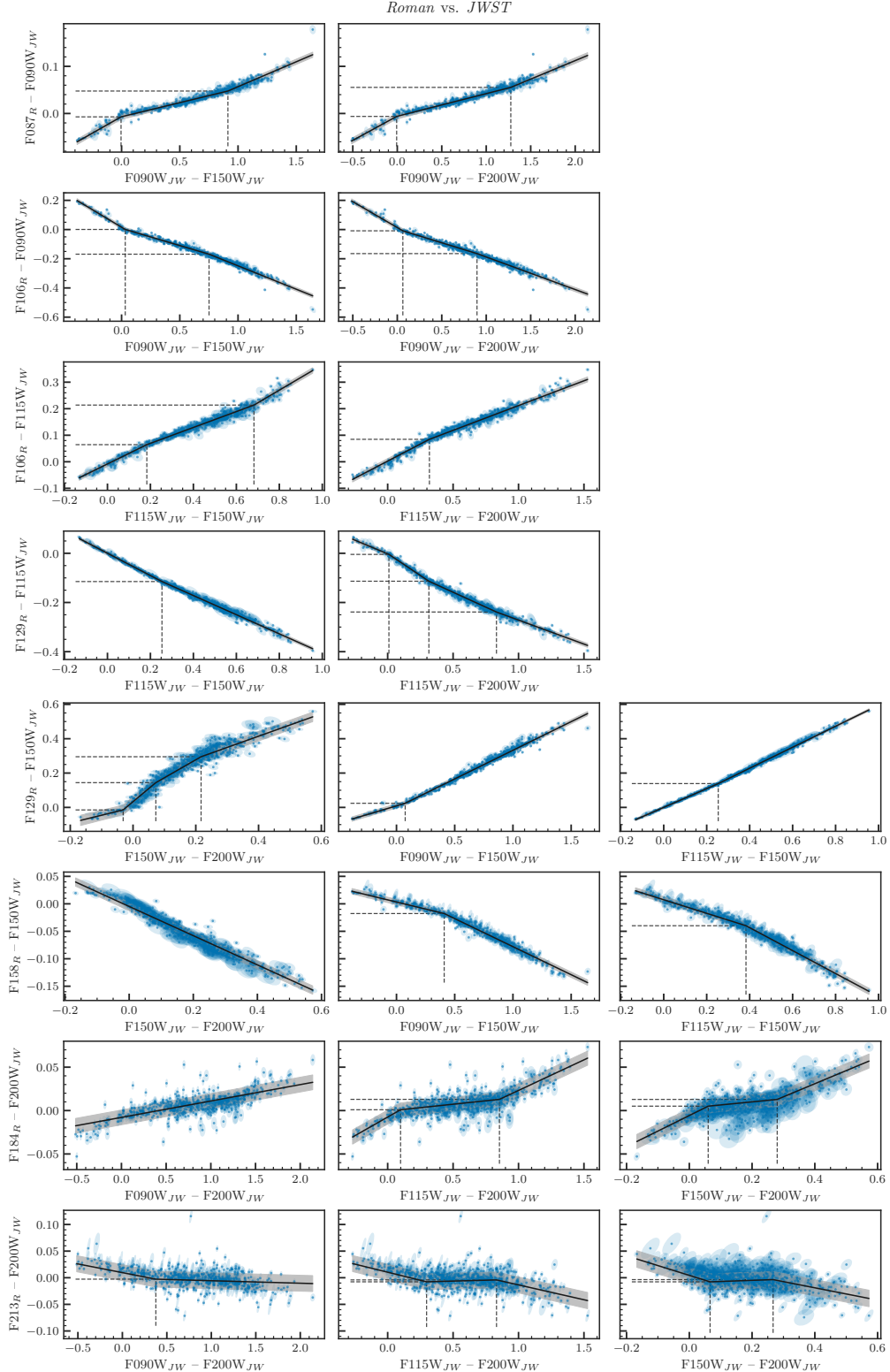


Figure 14. As Figure 5 for converting JWST filters to Roman.